Solar RRL
www.solar-rrl.com

Loss Analysis of Fully-Textured Perovskite Silicon Tandem Solar Cells: Characterization Methods and Simulation toward the Practical Efficiency Potential

Oussama Er-raji, Christoph Messmer,* Alexander J. Bett, Oliver Fischer, Sebastian Kasimir Reichmuth, Florian Schindler, Martin Bivour, Oliver Schultz-Wittmann, Juliane Borchert, Martin Hermle, Jonas Schön, Friedemann D. Heinz, Martin C. Schubert, Patricia S. C. Schulze, and Stefan W. Glunz*

Optimally enhancing the performance of perovskite silicon tandem solar cells comes with accurate identification of loss origins in the device in combination with optoelectrical device simulations assessing the respective efficiency gains to prioritize optimization pathways. Herein, various characterization methods, namely, spectrally resolved photoluminescence (PL), transient-PL, PL-based implied open-circuit voltage (iV_{OC}) imaging, spectrometric characterization, and Suns-V_{OC} measurements are combined to quantify current density–voltage (jV) photovoltaic metric losses of a fully-textured perovskite silicon tandem solar cell (26.7% efficiency). The extracted device characteristic parameters are then used as a reference for the comprehensive optoelectrical Sentaurus simulation model which precisely reproduces the experimentally obtained optical and electrical solar cell characteristics, considering mobile ion dynamics. Subsequently, starting from the current device design, the authors alleviate one step at a time the loss constraints and show the impact of each loss channel on the efficiency, the impact of each loss channel on the efficiency, identifying the three major ones to be at the: 1) perovskite/C_{60} interface ($-4.6\%_{abs}$) , 2) the series resistance ($-2.9\%_{abs}$), and 3) light management ($-2.1\%_{abs}$), which limit the V_{OC}, fill factor, and j_{SC} of the device, respectively. Furthermore, it is demonstrated that a practical efficiency potential of 39.5% can be regarded as a practical limit for the presented tandem device architecture.

1. Introduction

Perovskite silicon tandem solar cells can exceed the power conversion efficiency (PCE) of traditional silicon solar cells with only a little additional production costs, making them a promising candidate for photovoltaic (PV) deployment.[1–5] Over the past few years, tremendous efforts have been put into the development of compatible wide-bandgap perovskite absorbers with excellent bulk and interfacial quality as well as suitable charge transport layers, leading to high open-circuit voltage (V_{OC}) and fill factor (FF) devices.[6–10] Besides, the adoption of a textured-front silicon substrate provided a supplementary boost in the short-circuit current density (j_{SC}),[11–21] culminating in a device record PCE > 33%.[22] To further improve the performance of perovskite silicon tandem solar cells, it is crucial to identify performance limitations and localize both global and local loss mechanisms quantitatively.

Several studies have investigated loss mechanisms encompassing optical and/or electrical effects in perovskite silicon tan-

O. Er-raji, C. Messmer, A. J. Bett, O. Fischer, S. K. Reichmuth, F. Schindler, M. Bivour, O. Schultz-Wittmann, J. Borchert, M. Hermle, J. Schön, M. C. Schubert, P. S. C. Schulze, S. W. Glunz
Division Photovoltaics (PV)
Fraunhofer Institute for Solar Energy Systems ISE
Heidenhofstr. 2, 79110 Freiburg, Germany
E-mail: Oussama.er-raji@ise.fraunhofer.de; Christoph.messmer@ise.fraunhofer.de

O. Er-raji, C. Messmer, O. Fischer, S. K. Reichmuth, J. Borchert, J. Schön, F. D. Heinz, S. W. Glunz
Chair of Photovoltaic Energy Conversion
Department of Sustainable Systems Engineering (INATECH)
University of Freiburg
Emmy-Noether-Str. 2, 79110 Freiburg, Germany

The ORCID identification number(s) for the author(s) of this article can be found under https://doi.org/10.1002/solr.202300659.

© 2023 The Authors. Solar RRL published by Wiley-VCH GmbH. This is an open access article under the terms of the Creative Commons Attribution-NonCommercial-NoDerivs License, which permits use and distribution in any medium, provided the original work is properly cited, the use is non-commercial and no modifications or adaptations are made.

DOI: 10.1002/solr.202300659

dem solar cells.[9,23–25] For instance, Bett et al. used spectrometric characterization method to analyze j_{SC} losses due to current mismatch in a monolithic tandem cell and determine accurately the current matching point.[24] In a study by Farag et al. photoluminescence quantum yield measurements were carried out to reveal voltage losses at the interfaces as well as in the bulk of solution-processed perovskite thin films on textured silicon (with <1 μm pyramid height).[23] To analyze FF losses, Al-Ashouri et al. used injection-dependent absolute electroluminescence spectroscopy to reconstruct the individual perovskite silicon subcell jV curves without the influence of series resistance (R_S), which enabled estimating the efficiency potential if transport losses due to R_S can be avoided.[6] Furthermore, Boccard et al. implemented a two-diode model describing a perovskite silicon tandem cell and investigated the effects of series resistance, parallel resistance, and local defects on the device's FF.[26] Similarly, Zeng et al. followed a comparable methodology but extended their study to investigate supplemental efficiency-loss mechanisms of the tandem cell via circuit modeling.[27] However, for optimal solar cell development, experimentally identified loss mechanisms must be coupled with optoelectrical device simulations to assess efficiency gains and prioritize optimization pathways.

Furthermore, with the perspective of a future industrialization of the promising perovskite silicon tandem solar cell technology, it is crucial to determine the practical efficiency potential on the device level (i.e., before module integration) and under standard AM1.5G measurement condition. Here, we focus on the fully-textured perovskite silicon tandem solar cell architecture, where the perovskite absorber uniformly coats micrometer-sized pyramids. Due to the fully textured front, this architecture offers the best light management scheme, thus representing the most attractive perovskite silicon tandem for future PV deployment.[28] Nevertheless, to uniformly form perovskite on micrometer-sized pyramids, standard wet-chemical techniques are not suitable.[11] Instead, the hybrid evaporation/spin-coating method is the state-of-the-art.[11] With this difference in processing technique as well as the formation on a highly rough substrate, the perovskite crystallization is expected to change, and new particular loss origins arise.

The aim of this work is to evaluate the sources of voltage, current, and fill factor deficiency in a fully-textured perovskite silicon tandem solar cell, and demonstrate its practical efficiency potential through an extensive simulation model using experimentally determined solar cell characteristics. By performing absolute and transient photoluminescence (PL) measurements, PL-based iV_{OC} imaging, spectrometric characterization, and Suns-V_{OC} measurements, performance limitations are identified, and the cell's characteristic parameters, e.g., pseudo-fill factor, implied open-circuit (OC) voltage, and series resistance among others, are extracted. Through this, a comprehensive optoelectrical simulation study is carried out. The implemented model (in Sentaurus technology computer-aided design (TCAD)) precisely reproduced the optical and electrical solar cell characteristics taking into account mobile ion dynamics. With that, the impact of resolving the device limitations on the tandem's efficiency is elaborated. We calculated the efficiency improvements by going step-by-step from the experimentally realized cell with 26.7% to an idealized scenario reaching a practical efficiency potential of 39.5% which can be regarded as the upper bound for the presented fully-textured perovskite-silicon tandem device architecture.

2. Results and Discussion

2.1. Fabrication of a Fully-Textured Perovskite Silicon Tandem Solar Cell

The realized tandem solar cell consists of a p–*i*–n perovskite solar cell on top of a both-side textured heterojunction silicon solar cell (**Figure 1**a). The bottom solar cell features a random pyramid distribution with an average pyramid height of 1.5 μm as derived via laser scanning confocal microscope measurements (Figure S1, Supporting Information). The electrical connection between the two subcells is ensured via a 20 nm thick indium tin oxide (ITO) recombination layer. The ≈630 nm thick perovskite absorber is based on a double cation double halide formulation with an estimated $FA_{0.85}Cs_{0.15}Pb(I_{0.78}Br_{0.22})_3$ composition and a ≈1.67 eV bandgap. It is processed via the hybrid evaporation/spin-coating route to ensure a conformal formation on top of textured silicon.[29] The adjacent charge transport layers are [2-(9*H*-carbazol-9-yl)ethyl] phosphonic acid (2PACz) deposited via spin coating from a 7 mmol solution and evaporated C_{60} for hole and electron extraction, respectively. On top of the electron transport layer (ETL), a 20 nm thin tin oxide (SnO_x) buffer layer, deposited via atomic layer deposition, serves as a protection from sputter damage of the subsequent ITO window layer. Metallization is done using silver (Ag) electrodes through a nominal 1 cm^2 shadow mask. Finally, a 100 nm thick evaporated MgF_x layer is deposited to increase light incoupling into the device.

A cross-section scanning electron microscope (SEM) image showcases the conformal top-cell on the textured front silicon bottom solar cell (Figure 1b). The fully-textured perovskite silicon tandem solar cell delivers a stabilized 26.7% PCE when operated at a fixed voltage close to the maximum power point (Figure S2,

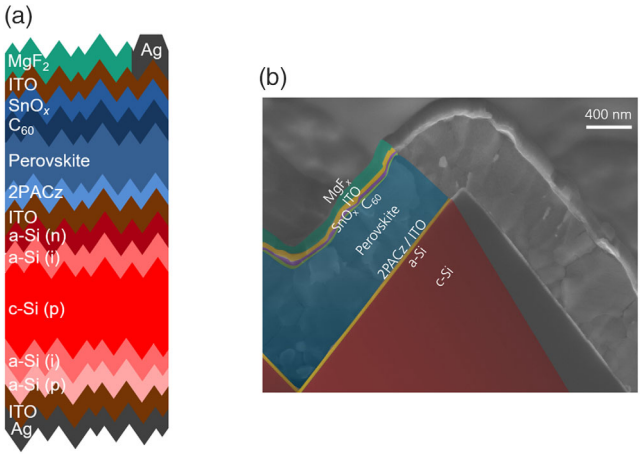

Figure 1. Implementation of a monolithic fully-textured perovskite-silicon tandem solar cell. a) Schematic of the monolithic tandem solar cell architecture. b) Cross-section SEM image of a fully-textured perovskite silicon tandem solar cell.

© 2023 The Authors. Solar RRL published by Wiley-VCH GmbH

2367198x, 0, Downloaded from https://onlinelibrary.wiley.com/doi/10.1002/solr.202300659 by Fraunhofer Ise Inst. Solar Energy Systems, Wiley Online Library on [16/11/2023]. See the Terms and Conditions (https://onlinelibrary.wiley.com/terms-and-conditions) on Wiley Online Library for rules of use; OA articles are governed by the applicable Creative Commons License

Supporting Information). In contrast to state-of-the-art fully-textured perovskite silicon tandems, we note that no crystallization nor bulk defect passivation agent was implemented in the perovskite absorber and no additional passivation layer was implemented between the perovskite/C_{60} interface (typically LiF). As a result, a lower solar cell efficiency is obtained, but a higher stability can be expected.[14,16,30,31]

2.2. Characterization and Loss Analysis of the Tandem Solar Cell

2.2.1. Open-Circuit Voltage (V_{OC}) Loss Analysis by Absolute PL, PL-Based iV_{OC} Imaging, and Transient PL

To boost the V_{OC}, voltage losses due to nonradiative recombination (charge carriers' recombination at, e.g., bulk or surface-/interface-related defects) as well as limited selectivity (resistance experienced by electrons and holes as they travel through the absorber and out of the contact layers) need to be reduced. By performing absolute spectrally resolved photoluminescence measurements in between different processing steps of the perovskite top-cell stack, we determine its iV_{OC} potential and highlight the main origins of carrier recombination losses (**Figure 2**a). Following that, we assess the total iV_{OC} of the perovskite silicon tandem device (from subcell selective PL-based iV_{OC} imaging) to understand to what extent carrier selectivity losses reduce the OC voltage from iV_{OC} to V_{OC}.[32,33]

Figure 2b shows that before deposition of the ETL, the perovskite/2PACz/ITO/textured silicon stack exhibits an iV_{OC} of (1210 ± 2) mV (note here that in this case silicon is not photoactive and is rather used as a substrate to provide the textured morphology; similar laser intensity applied for all layer stacks in Figure 2a neglecting optical influence of added layers). Given the 1.374 V radiative limit of a semiconductor with a 1.67 eV bandgap,[34] we calculate a voltage deficit of ≈155 mV attributed to nonradiative recombination losses in the bulk of the polycrystalline perovskite film and the perovskite/hole transport layer (HTL) interface. As self-assembled monolayers,

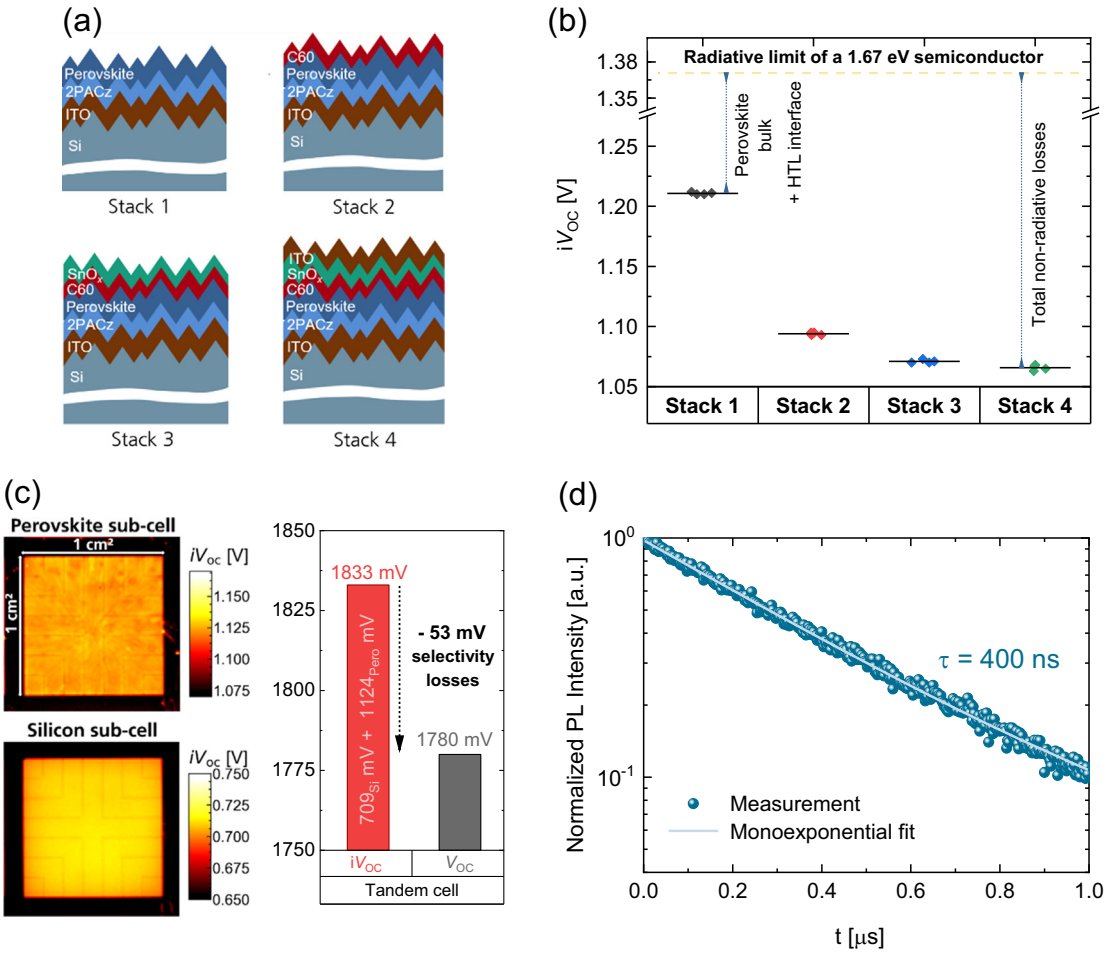

Figure 2. Voltage loss analysis of the established fully-textured perovskite silicon tandem solar cell. a) Top perovskite subcell stacks used for investigation. b) Implied OC voltage (iV_{OC}) losses due to nonradiative recombination at the perovskite bulk and at the interfaces (via absolute spectrally resolved PL measurements) of the stacks in (a). c) iV_{OC} images of the perovskite top cell and silicon bottom cell extracted from PL images of the subcells. The bar graph shows the comparison between iV_{OC} (sum of mean iV_{OC} in silicon and perovskite subcells) and V_{OC} of the device (measured directly afterward). d) Transient PL measurement to extract charge carrier lifetime which is used for electrical simulation (cf. Section 2.3.1. (measurement carried out on stack 1 in (a)).

© 2023 The Authors. Solar RRL published by Wiley-VCH GmbH

2367198x, 0, Downloaded from https://onlinelibrary.wiley.com/doi/10.1002/solr.202300659 by Fraunhofer Ise Inst. Solar Energy Systems, Wiley Online Library on [16/11/2023]. See the Terms and Conditions (https://onlinelibrary.wiley.com/terms-and-conditions) on Wiley Online Library for rules of use; OA articles are governed by the applicable Creative Commons License

particularly 2PACz, have been previously found to induce minimal nonradiative recombination losses at the perovskite/HTL junction, we ascribe the majority of the determined iV_{OC} drop to the polycrystalline perovskite bulk.[6,9,35] Upon addition of the C_{60} layer, an additional drop of (115 ± 2) mV is observed compared to the previous stack. Since the evaporation of C_{60} at low rates (0.15 Å s^{-1}) does not damage the perovskite, we attribute the observed drop to high nonradiative recombination at the perovskite/C_{60} junction, as has been previously reported.[36–39] The perovskite/C_{60} interface and the perovskite bulk constitute the largest deficit of voltage in the current tandem stack. Considering the incorporation of SnO_x buffer and ITO window layers (additional iV_{OC} loss of ≈40 mV), the overall nonradiative recombination losses in the perovskite subcell amount to (310 ± 3) mV.

Charge carrier selectivity losses in the tandem device, which cause a voltage drop from internal voltage (also called implied voltage or quasi-Fermi level splitting over charge) to external voltage,[40] were assessed via subcell PL-based iV_{OC} imaging.[33] Figure 2c shows the iV_{OC} distribution in the active area of the top and bottom cells. By summing up the average iV_{OC} of the pixels in the perovskite subcell area (1124 mV) as well as the silicon subcell area (709 mV) and comparing it to the V_{OC} of the device (1780 mV), a voltage loss $\Delta V_{OC} = iV_{OC} - V_{OC}$ of 53 mV was found. This results in a selectivity metric external/internal V_{OC}-ratio $\zeta = V_{OC}/iV_{OC} = 0.97$.[32,41]

The performed voltage loss analysis concludes that to reach the full V_{OC} potential, reducing nonradiative recombination losses, especially at the perovskite/ETL interface and perovskite bulk, should be prioritized before tackling the moderate selectivity losses.

2.2.2. FF Loss Analysis by Suns-V_{OC} Measurements

To estimate FF losses in the tandem solar cell, Suns-V_{OC} measurements were performed. By varying the illumination intensity and measuring V_{OC}, a pseudo-jV curve of the tandem solar cell was derived. As the measurement is conducted in OC conditions, i.e., with no current flowing in the device, the constructed pseudo-jV curve represents the jV curve of the solar cell without resistive losses.

By comparing the pseudo-jV curve to the jV curve (ion-quenched jV curve obtained after 3 h under illumination at OC conditions as will be further described in the simulation section), we noted a large difference of nearly $10\%_{abs}$ between the FF (74.2%) and the pseudo fill factor (pFF = 84%), which corresponds to a series resistance (R_S) of $\approx 9\,\Omega\,cm^2$ (**Figure 3**). This shows that the tandem device has an FF potential of 84% if transport losses stemming from: 1) charge transport in the perovskite absorber; 2) charge transport across interfaces; and 3) series resistance at different interfaces in the tandem stack are alleviated. Out of the three possible contributions, we suspect the nonoptimal charge transport at the perovskite/2PACz interface to have the largest impact on the high R_S. In this junction, remnant PbI_2 tends to accumulate when using the hybrid evaporation/spin-coating perovskite processing technique (originating from a nonoptimal evaporated scaffold to perovskite conversion), which can hamper charge extraction and lead to an increased series resistance.[42] X-ray diffractogram measurements of the perovskite absorber confirm the presence of an additional PbI_2 (001) peak besides the characteristic perovskite cubic phase, as shown in Figure S3, Supporting Information.

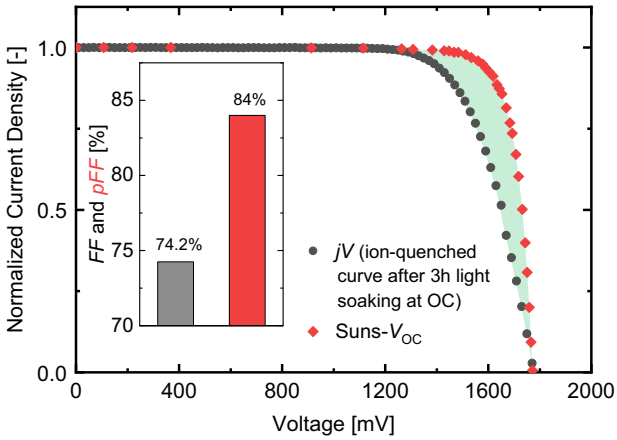

Figure 3. FF loss analysis performed by comparing the current density–voltage (jV) and pseudo-jV curve (constructed from Suns-V_{OC} measurements) of the tandem solar cell. The inset indicates the difference between the FF and pseudo-FF.

From this perspective, further improving the perovskite crystallization with the hybrid route, to form a PbI_2-free perovskite/HTL interface, is expected to enhance charge extraction and ultimately boost the tandem cell's FF.

2.2.3. Short-Circuit Current Density (j_{SC}) Loss Analysis by Spectrometric Characterization

Regarding j_{SC} losses, the adopted two-terminal tandem solar cell configuration dictates that the highest short-circuit current density can be obtained at the current matching point. If one of the two subcells delivers a lower photogenerated current, it limits the j_{SC} (assuming no significant parallel resistance in the limiting subcell). Besides current mismatch losses, parasitic absorption and reflection due to the differences in refractive index of the tandem stack layers further reduce the j_{SC} potential.

To determine the current matching point, spectrometric characterization is performed (**Figure 4**). This method has been described in detail for III–V tandem solar cells by Meusel et al.[43] and was recently also applied for perovskite silicon tandem devices.[24,44,45] In spectrometric characterization, the spectrum is systematically varied and for each spectral condition, a jV curve is recorded. Each spectral condition is assigned a parameter z according to the following equations: $j_{top}^{sim} = (1+z) \cdot j_{top}^{ref}$ and $j_{bot}^{sim} = (1-z) \cdot j_{bot}^{ref}$.[43] j_{top}^{sim} and j_{bot}^{sim} are the photocurrents of the top and bottom solar cell, respectively, j_{top}^{ref} and j_{bot}^{ref} denote the corresponding currents under the reference spectrum, i.e., the Air Mass 1.5 global (AM1.5G) spectrum in this case. $1+z=1$ corresponds to the AM1.5G condition, for $1+z<1$ the spectrum is redshifted, and for $1+z>1$ the spectrum is blueshifted compared to the AM1.5G spectrum. In an ideal case, when the limiting subcell shows a flat jV characteristic for low voltages,

© 2023 The Authors. Solar RRL published by Wiley-VCH GmbH

2367198x, 0, Downloaded from https://onlinelibrary.wiley.com/doi/10.1002/solr.202300659 by Fraunhofer Ise Inst. Solar Energy Systems, Wiley Online Library on [16/11/2023]. See the Terms and Conditions (https://onlinelibrary.wiley.com/terms-and-conditions) on Wiley Online Library for rules of use; OA articles are governed by the applicable Creative Commons License

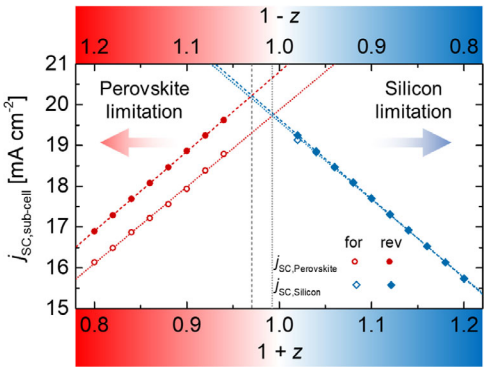

Figure 4. Spectrometric characterization of the tandem solar cell. The current matching (gray lines) is determined by linear fits (colored lines) to the subcell j_{SC} values depending on the spectral condition. Points close to the maximum are not considered for the fit and therefore not represented. Due to dynamic effects in the perovskite, the current matching was determined from values obtained from forward (dotted lines) and reverse scans (dashed lines). In both cases, current matching is reached for redshifted spectra compared to the AM1.5G spectrum ($1+z=1$), which means that the silicon solar cell is limiting at the AM1.5G condition.

the photocurrent of the limiting subcell equals the j_{SC} of the tandem device. However, when the limiting subcell has a low parallel resistance or a low breakthrough voltage, this is not true anymore. As for redshifted spectra, the jV curves were not flat for low voltages (Figure S4, Supporting Information); to analyze current matching, the subcell current density $j_{SC,subcell}$ of the limiting subcell is shown in Figure 4. To determine $j_{SC,subcell}$, a constant voltage of the silicon subcell of 700 mV has been assumed (An exact determination of a subcell V_{OC} in the tandem device is difficult. This value is in the range of the measured iV_{OC} of 709 mV, see Figure 2c. Furthermore, a deviation of ≈20 mV would not affect the position of the current matching point significantly). $j_{SC,Silicon}$ was then determined at $V = V_{OC,tandem} - 700$ mV on the tandem jV curve. As for perovskite limitation, the tandem jV curve shows a hysteresis in V_{OC}, no constant perovskite voltage could be assumed, but the values for $j_{SC,Perovskite}$ were taken at $V = 700$ mV (assuming that the dynamic effects leading to hysteresis are coming from the perovskite while the silicon has a constant voltage). Considering the $j_{SC,subcell}$ values of the limiting subcell, the current matching was determined by the intercept of two linear fits (one to the $j_{SC,Perovskite}$ values for the red-rich spectral conditions and one to the $j_{SC,Silicon}$ for the blue-rich spectral conditions, each for the linear part of the $j_{SC,subcell}$ values). Points very close to the current matching point were not considered for the fits, more details can be found in Figure S4c, Supporting Information. The current matching points are at $1+z=0.97$ and $1+z=0.99$ when using the $j_{SC,subcell}$ values from reverse scans (V_{OC} to I_{SC} sweep) and forward scans (I_{SC} to V_{OC} sweep), respectively. Due to dynamic effect leading to hysteresis in the perovskite, a unique current matching point cannot be determined from the jV scans. However, current matching is reached for $1+z<1$ in both cases (for values obtained from forward and reverse scan) which means that the spectrum needs to be redshifted compared to the AM1.5G spectrum to reach current matching and thus, the silicon solar cell is current limiting at the AM1.5G condition. A strong decrease in hysteresis can be seen around the current matching point, which cannot be explained by simple jV curve addition of the subcells. More details can be found in the study of Messmer et al.[46]

Besides current matching, reflection and parasitic absorption can further reduce the generated short-circuit current density. While reflection losses are reduced by implementing the fully-textured tandem cell design (reduction in reflection equivalent current from 3.1 to 1.0 mA cm^{-2} for flat compared to fully-textured tandem design[47]), we assess the parasitic absorption by performing reflection transmission measurements on the top C_{60}/SnO_x/ITO contact layers. Out of the three layers, the absorption spectrum of the ETL C_{60} is found to be the main source of curtailment of the useful light in the perovskite absorber (Figure S6, Supporting Information).

The performed j_{SC} loss analysis (current matching, parasitic absorption) concludes that it is possible to achieve a higher current by either reducing the perovskite thickness or increasing its bandgap (for current matching), in addition to minimizing parasitic absorption through a reduced C_{60} thickness. We note that increasing the perovskite bandgap would be favorable as it would lead to a supplemental increase in V_{OC} if the perovskite quality is preserved (e.g., no halide segregation).

2.3. Optoelectrical Simulation of the Perovskite-Silicon Tandem Cell

2.3.1. Modeling Approach and Experimental Validation of the Optical Model

To further analyze the results of the experimental loss analysis, a comprehensive optoelectrical model of the current perovskite-silicon tandem cell was set up to show the impact of the present limitations on the tandem efficiency and to derive the practical efficiency potential of this device architecture. The optical model was set up in Sentaurus TCAD[48] and validated for planar front-side devices in previous publications.[45,49] It is based on ray tracing in the crystalline silicon absorber and transfer matrix method for the top and bottom cell thin-film layer stacks (including the perovskite). This model was explained in several previous publications.[49–51] In this section, we show the adaptations we made within the scope of this article to obtain an optical model for fully front- and rear-side textured perovskite-silicon tandem devices.

Figure 5 shows the results as a comparison between the experimental data (scaled external quantum efficiencies (EQEs), see dotted lines) as published in ref. [42] and the optical simulation data (absorption, see solid lines) for the fully-textured tandem device of Figure 1a. The perovskite thickness was assumed to be 630 nm which is in good agreement with the targeted and measured thickness of approximately 630 nm determined by SEM cross-section images of the experimental device (Figure 1b). The green lines in Figure 5 show the total absorption (i.e., 1-reflection). The simulation data matches the experimental data very well despite minor deviations. The reflection caused by the ≈2% metallization area was considered in the simulation model.

© 2023 The Authors. Solar RRL published by Wiley-VCH GmbH

2367198x, 0, Downloaded from https://onlinelibrary.wiley.com/doi/10.1002/solr.202300659 by Fraunhofer Ise Inst. Solar Energy Systems, Wiley Online Library on [16/11/2023]. See the Terms and Conditions (https://onlinelibrary.wiley.com/terms-and-conditions) on Wiley Online Library for rules of use; OA articles are governed by the applicable Creative Commons License

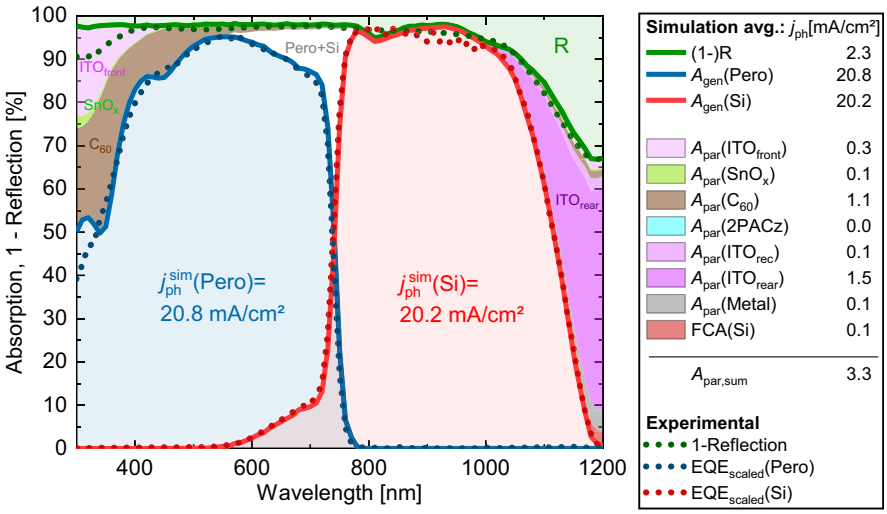

Figure 5. Simulated absorption of the perovskite (blue) and silicon (red) absorber, as well as the parasitic layer losses in each layer of the perovskite-silicon tandem device as in Figure 1a; the simulated absorption and reflection curves show a very good agreement to the experimental data (dotted lines).

The measured EQE of the silicon bottom cell (dotted red) and the simulated absorption in the silicon wafer A(Si) (solid red) show good agreement, except for slight deviations around 950 nm. Overall, the integrated photocurrent density of the simulated silicon EQE with $j_{ph} = 20.2\ \mathrm{mA\,cm^{-2}}$ confirms the current limitation of the tandem device with a measured j_{sc} value of 20.2 mA cm^{-2} (as shown in the next subsection).

The dotted blue line shows the measured EQE of the perovskite cell EQE(Pero) in comparison with the simulated absorption within the perovskite A(Pero), shown as a solid blue line. The experimental EQE was scaled to the height of the simulation since the experimental EQE of a tandem device is usually only measurable with a relative height.[52] One can see that the simulated A(Pero) describes the shape of the EQE(Pero) quite well, however, there are minor deviations in the short wavelength regime. One can see that the simulated perovskite data show distinct local minima and maxima from 300 to 500 nm which is characteristic for the optical data of C_{60}, in this case taken from the study of Sittinger et al.[53] In the measured EQE, this characteristic is visible but much less prominent. This difference could arise from a C_{60} thickness that is lower than the target thickness of 15 nm for the device, as it was used for the simulation.

Overall, we see a very good agreement between our simulation model and the experimentally measured data that further underlines the validity of our model. Moreover, Figure 5 highlights the respective parasitic absorption losses in each layer as derived from the simulation model. One can see that the dominant parasitic losses are given by the C_{60}, the front, and rear ITO layers, with a parasitic loss in photocurrent of about 1.1, 0.3, and 1.5 mA cm^{-2}, respectively. To estimate the practical efficiency potential of this device architecture, we will adapt the actually present optical properties, as shown in Figure 5. The aim is to increase the tandem photocurrent to an idealized scenario where layer thicknesses are minimized, but still present (which will be used as "improved optics" at the end of this section). The steps are:

The C_{60} layer thickness is reduced from 15 to 5 nm which should be close to the thinnest possible layer that is still electrically functional (only above 5 nm we expect a closed film formation[54]).

The more transparent rear-side ITO was implemented since no lateral conductivity is needed for this monofacial device, a less conductive, thus, a more transparent ITO composition was used.

The ITO thicknesses of front and recombination ITO were reduced from 25 to 15 nm, and 20 nm to 10 nm, respectively, and the SnO_x thickness was reduced from 20 to 5 nm.

To achieve current matching between the two subcells, the perovskite's bandgap was altered from currently 1.670 eV to now 1.692 eV (whereby the last digit would be within the experimental uncertainty but can be fine-tuned very well in the simulation model).

Only the active area of the cell is considered without perimeter losses and without reflection losses due to metallization (instead of 2% metallization area as in Figure 5). For full-sized wafer-based tandem cell and modules, we expect optoelectrical trade-offs when optimizing the front electrode.[55]

With these optical adaptations applied to Figure 5, the photocurrent of both perovskite and silicon subcell increases to 21.34 mA cm^{-2} (not shown). This result is used as "improved optics" in the following sections.

2.3.2. Electrical Modeling

The full optoelectrical model used in this article was experimentally validated by Messmer et al.[46] It includes all electrically active layers that are shown in Figure 1a, and is capable to describe the perovskite top cell in very sophisticated detail based on drift-diffusion equations including the mobile anions and cations within the perovskite (for simulation details, refer to ref. [46]). As drift-diffusion modeling has a large number of input parameters; the parameter choices that are relevant for validating

© 2023 The Authors. Solar RRL published by Wiley-VCH GmbH

2367198x, 0, Downloaded from https://onlinelibrary.wiley.com/doi/10.1002/solr.202300659 by Fraunhofer Ise Inst. Solar Energy Systems, Wiley Online Library on [16/11/2023]. See the Terms and Conditions (https://onlinelibrary.wiley.com/terms-and-conditions) on Wiley Online Library for rules of use; OA articles are governed by the applicable Creative Commons License

this TCAD model were made according to the measurement data as derived from the characterization part of this article. This ensures that the results derived from the model are based on realistic assumptions. However, the origin of loss channels might be ambiguous and have to be handled with care. Accordingly, this model was adapted to the experimental device of this work by implementing the loss channels based on the measured limitations of Section 2.2.

An internal voltage iV_{OC} of the silicon subcell of about 726 mV at the illumination equivalent to the AM1.5G spectrum taking into account the absorption of the top cell by assuming a surface recombination velocity (SRV) of 100 cm s^{-1} at the silicon heterojunction contacts.

A lifetime within the perovskite bulk of 400 ns, as measured via transient photoluminescence for the composition of our perovskite absorber (see Figure 2d).

A surface recombination at the 2PACz layer that lowers the internal voltage iV_{oc} of the perovskite absorber to about 1.24 V, which is close to the measured value of Stack 1 in Figure 2b.

A conduction band misalignment of the perovskite/C_{60} interface of about 0.25 eV as based on Menzel et al.[54] combined with a SRV of $6{\cdot}10^4$ cm s^{-1} to achieve an iV_{oc} drop of roughly 100 mV in the perovskite absorber due to nonradiative recombination at the ETL.

An (external) series resistance of 9 Ω cm^2 which corresponds to the drop of the pFF (the simulated value is 87% which is a 3% higher than the measured pFF) to FF, as shown in Figure 3.

The mobile ions of our device were determined to be roughly 6×10^{16} cm^{-3} (not shown here but in an upcoming publication).

Figure 6a shows the "ion-quenched *jV* curves" for both simulation (orange line) and experiment (green dots). A preconditioning of 3 h under illumination at 1 sun and OC conditions was performed in both simulation and experiment. Afterward, the experimental *jV* curve was obtained by jumping back and forth between each measurement point (shown in green dots) and OC conditions. The holding time at OC is significantly longer than at the measurement point, therefore the ions can be expected to be kept at their OC conditions. In the simulation, the ion-quenching was effectively achieved by using a short scan time of 5 s which is too low for the ions to move from their OC conditions. It is worth mentioning that due to the high ion density of 6×10^{16} cm^{-3}, the device shows significant FF hysteresis when performing "standard" reverse and forward *jV* scans. We ascribe this to the incomplete perovskite conversion as described in Section 2.2.2. For the loss analysis carried out in this article, it is however very reasonable to analyze the losses for what we call "ion-quenched *jV* curves," as for OC-quenching of ions, the anion (cation) concentration at the ETL (HTL) interface is expected to be comparable to under operation. (Note that the reverse *jV* scan is almost equal to the ion-quenched *jV* curve if the scan speed is sufficiently high, e.g., smaller than 90 s.) One can see that the simulated *jV* curve describes the experimental data very well.

Figure 6b shows the band diagram of the simulated perovskite-silicon tandem device at V_{OC} after 3 h of light-soaking at OC conditions. One can see the quasi-Fermi level splitting of both perovskite and silicon absorber, which correspond to their respective internal voltages. The undesired gradient of the electron quasi-Fermi level within the perovskite absorber toward

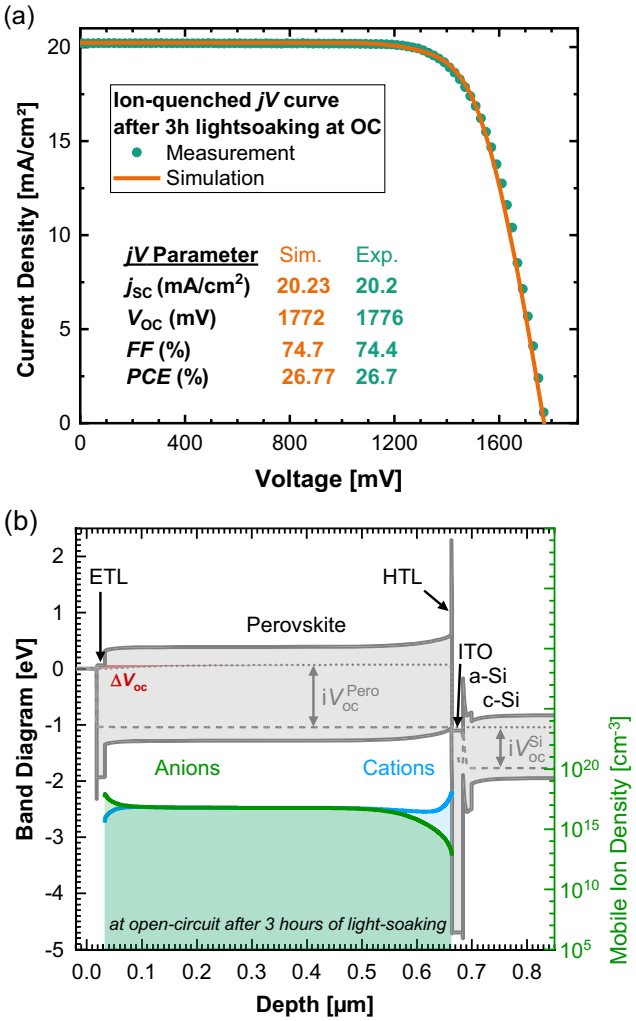

Figure 6. a) Ion-quenched *jV* curve after 3 h of light-soaking at OC conditions for both measured (green) and simulated (orange) perovskite-silicon tandem device showing a very good agreement of the optoelectrical model with the experimental cell. b) Band diagram of the perovskites-silicon tandem device at OC after 3 h of light-soaking. The (undesired) gradient of the electron quasi-Fermi level is highlighted in red, causing a voltage drop of $\cdot V_{OC} = iV_{OC} - V_{OC}$.

the C_{60} transport layer is highlighted in red, causing a voltage drop of $\Delta V_{OC} = iV_{OC} - V_{OC} = 56$ mV. This matches very well the measured ΔV_{OC} value of 53 mV, shown in Figure 2c.

2.3.3. Toward the Practical Efficiency Potential of Perovskite Silicon Tandem Devices

Finally, taking Figure 5 and 6 as optical and electrical starting point, respectively, which represents the current status of our tandem device, we now elaborate for each loss channel on how the tandem efficiency would be enhanced when each corresponding electrical limitation would be completely resolved. In a real cell, this would only partly be possible, so that the values should be regarded as an idealized scenario. As from an optical

© 2023 The Authors. Solar RRL published by Wiley-VCH GmbH

2367198x, 0, Downloaded from https://onlinelibrary.wiley.com/doi/10.1002/solr.202300659 by Fraunhofer Ise Inst. Solar Energy Systems, Wiley Online Library on [16/11/2023]. See the Terms and Conditions (https://onlinelibrary.wiley.com/terms-and-conditions) on Wiley Online Library for rules of use; OA articles are governed by the applicable Creative Commons License

point of view, the parasitic absorption would be best for no contact layers at all, which is why we do not refer to an "ideal" optics, but only to an "optimized" optical scenario as introduced before. While the Shockley–Queisser (SQ) limit[56] is unambiguously defined (and can be calculated to be 45.2% for this device featuring a 1.12 eV bottom cell bandgap), the definition of a "practical limit" of perovskite-silicon tandem devices is much more ambiguous as it depends on the choice of technological boundary conditions. There are several attempts in the literature to assess a "practical potential" for multijunction solar cells.[2,25,57] Futscher et al. modeled the performance limitations of perovskite silicon tandem solar cells under realistic operating conditions and calculated that for an optimized scenario, perovskite silicon tandem solar cells "could reach efficiencies above 38%".[2] More theoretical approaches, like Almansouri et al. calculated a "best efficiency limit" for perovskite silicon tandem solar cells of 40.6% based on SQ limit extended by incorporating further assumptions on optical and electrical losses like complete absorption within the perovskite due to finite film thickness or reflection from the glass.[57] However, in this work, we focus on the R&D on the cell level based on a full optoelectrical model adapted to a real device based on experimentally characterized input parameters. By mitigating the previously discussed loss channels, we showcase the practical efficiency potential for a fully-textured perovskite-silicon tandem device architecture. **Figure 7** shows the tandem efficiency for cumulatively mitigated loss channels, chosen in an order that first *FF*, second V_{OC}, and third j_{SC} losses are diminished (for a roadmap and experimentally these steps would be tackled in a different order however), ultimately reaching the practical efficiency potential of this tandem architecture which we assess to be at 39.5%.

The starting point is the current status as presented in this work (see green star at 1) with a tandem efficiency of 26.7%.

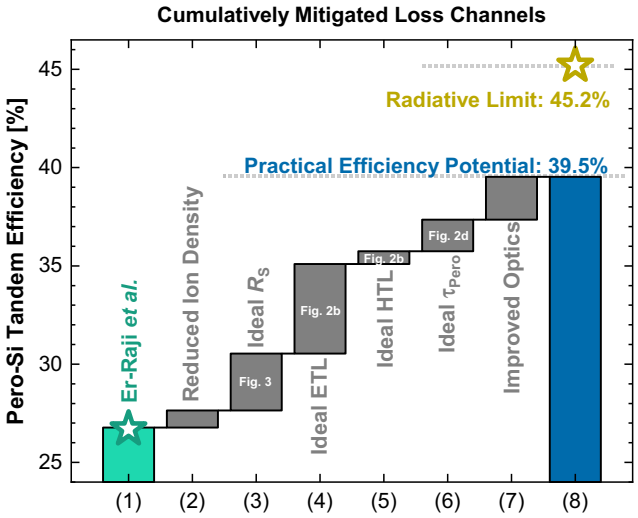

Figure 7. Optoelectronic simulation of the perovskite-silicon tandem cell and cumulatively mitigated loss channels and their respective efficiency gains toward the practical efficiency potential of 39.5% as determined by this work. Most steps are based on the characterization methods and obtained experimental values as presented in this article (see figure numbers within the bars).

Step 2 shows the impact of a lowered ion density in the perovskite absorber (from measured $6 \times 10^{16}\,\mathrm{cm}^{-3}$ to lower $1 \times 10^{16}\,\mathrm{cm}^{-3}$, which is not limiting the FF anymore) which has positive impact on the FF but also lowers the hysteresis effects on reverse and forward *jV* scans (not shown here). This is due to the fact that a lower anions (cations) concentration leads to generally lower accumulation at the ETL (HTL) interfaces, which increases the selectivity of the respective contacts. The efficiency increases to 27.6%.

Step 3 shows the impact of solving the problem of the high external series resistance of about $9\,\Omega\,\mathrm{cm}^2$ that will improve the FF up until the pFF, as quantified in Figure 3. This would be related to a tandem efficiency increase of about $+2.9\%_{abs}$ to 30.5%.

In step 4, we show the improvement by solving the problem of high nonradiative recombination at the ETL, namely the C_{60}. The simulation model reveals that when undesired energetic conduction band offset of 0.25 eV is set flat band to the desired value of 0 eV for the C_{60}/Pero interface, the recombination losses at the ETL are almost completely resolved, despite the high SRV of $6 \times 10^4\,\mathrm{cm\,s}^{-1}$. If SRV is set to $0\,\mathrm{cm\,s}^{-1}$, another 20 mV is gained. One can see that solving the E_C offset at the C_{60}/Pero interface has the overall biggest impact, as it would boost the efficiency by $4.6\%_{abs}$ to 35.1%.

In step 5, we show the impact of improving the HTL to reach the iV_{oc} limit that we would expect for ideal ETL and HTL extraction layers. This was done by increasing the dipole moment of the 2PACz layer by one order of magnitude which leads to ideal hole extraction. As the voltage losses for the 2PACz layers are not as high as for the ETL, we see a smaller increase for ideal HTL properties of about $0.6\%_{abs}$ to 35.7%.

In step 6, we show the impact of a perovskite bulk lifetime of 1 ms (which corresponds to a nonlimited lifetime) instead of 400 ns. We see that the efficiency potential would be increased by another $1.7\%_{abs}$ to 37.4%. (In this step, we also set the silicon SRV to $0\,\mathrm{cm\,s}^{-1}$ which makes $0.2\%_{abs}$ out of the total improvement.)

Going toward step 7, we show the impact of the "improved optics" as previously discussed. The main effect relates to the current matching of the subcells. But also the reduced parasitic absorption due to thinner layers has positive impact on the current. This is expected to boost the efficiency by another $2.1\%_{abs}$ to 39.5%.

We refer to the final 39.5% tandem efficiency as "practical efficiency potential" for this device architecture (see gray dotted line in Figure 7). Optically, it can be only exceeded when finding different device architecture, e.g., by replacing C_{60} with a more transparent ETL and finding more transparent alternatives to the ITO layers. Electrically, this practical potential can be seen as an upper limit, since the resulting *jV* curve is only limited by Auger in the silicon bulk and the radiative recombination of the perovskite bulk leading to an (almost) ideal diode characteristic with a FF of about 90%. Therefore, experimental perovskite-silicon tandem devices will most likely lie below the 39.5% efficiency potential. Nevertheless, one can see that there is still a major efficiency gap between the practical potential and the radiative limit of 45.2% (see yellow star in Figure 3c) as derived from the SQ limit for a bottom cell with the 1.12 eV bandgap of silicon.[56] However, this is analogous to the single

© 2023 The Authors. Solar RRL published by Wiley-VCH GmbH

2367198x, 0, Downloaded from https://onlinelibrary.wiley.com/doi/10.1002/solr.202300659 by Fraunhofer Ise Inst. Solar Energy Systems, Wiley Online Library on [16/11/2023]. See the Terms and Conditions (https://onlinelibrary.wiley.com/terms-and-conditions) on Wiley Online Library for rules of use; OA articles are governed by the applicable Creative Commons License

junction world, where the 33.2% SQ limit is not reachable with silicon single junction as Auger recombination is the intrinsic limiting recombination path in silicon absorbers and these cells are limited to 29.4% (Niewelt et al.[58]). The practical efficiency limit would be thus lower for a silicon cell.

Despite the fact that this analysis shows a quite idealized scenario when solving the device limitations, it is still useful to assess the "ideal" efficiency boost for each limitation: one can see that the major issues within the device are first, the ETL limitation, second, the high series resistance limitation, and third, the optical improvements (i.e., mainly current matching). Some potential strategies to address these issues can be improving the V_{OC} by 1, applying a passivation layer such as MgF_x at the perovskite/C_{60} interface to reduce nonradiative recombination losses[36] and 2, applying a surface treatment that lowers the band alignment offset at the perovskite/C_{60} interface by locally changing the perovskite surface work function as has been previously demonstrated in highly efficient perovskite single junction solar cells[59]; reducing the solar cell internal series resistance by further improving the perovskite bulk's radiative quality and eliminating residual PbI_2 via, e.g., addition of Lewis-base crystallization agents in the solution step,[60] as well as enhancing the electron and hole conductivity at the respective extraction layers to avoid selectivity losses[61,62]; improving the tandem j_{SC} by increasing the perovskite bandgap and optimizing the thickness of functional layers.[63] These problems must be tackled to reach >35% for a perovskite-silicon tandem solar cell with a device architecture as presented in this work.

3. Conclusion

This work uses different characterization methods and numerical simulation to analyze the device losses and derives efficient pathways for optimization of monolithic fully-textured perovskite silicon tandem solar cells (where the perovskite film is processed via the hybrid evaporation/spin-coating route and conformally coats micrometer-sized pyramids). To do this, in the first step, a comprehensive loss analysis of a tandem cell is performed. In particular, high series resistance, current mismatch in the subcells, and high nonradiative recombination losses as well as band misalignment at the perovskite/ETL interface were identified to be the major performance limitations of the FF, j_{SC}, and V_{OC} of the device, respectively. In a second step, a sophisticated optoelectrical TCAD simulation model, which precisely reproduces both optical and electrical experimental observations of the performed loss analysis, was used to quantify the impact of the identified device limitations on the tandem jV metrics. This enabled assessing the efficiency drop due to the major loss mechanisms: 1) perovskite/C_{60} interface ($-4.6\%_{abs}$); 2) the series resistance ($-2.9\%_{abs}$); and 3) light management ($-2.1\%_{abs}$). By reducing the origins of these losses one step at a time, we calculated the efficiency improvements by cumulatively mitigating the characterized loss channels, ultimately reaching a practical efficiency potential of 39.5% for this device architecture. In conclusion, by combining various characterization methods to quantify losses in a tandem solar cell with an optoelectrical simulation model to assess the efficiency potential, this work provides a crucial guideline for optimal solar cell device optimization. Furthermore, the determined practical efficiency potential of the solar cell on the device level can serve as a basis for future research and development studies (e.g., cell-to-module analysis, investigation of module performance under real-world operating conditions, etc.) which are needed prior to the commercialization of the promising fully-textured perovskite silicon tandem solar cell technology.

4. Experimental Section

Characterization: Optical microscopy of surface texture: a 3D laser confocal microscope (LEXT OLS4000, Olympus) was used to characterize the random pyramids prepared on (100)-oriented crystalline Si bottom solar cells by an alkaline anisotropic etching solution. The obtained 3D surface texture was merged in a 2D plan view with a very large depth of field. The pyramid base area distribution was determined using in-house developed software as described in (T. Strauch, M. Demant, A. Lorenz, J. Haunschild and S. Rein, Two Image Processing Tools to Analyse Alkaline Texture and Contact Finger Geometry in Microscope Images, Proceedings of the 29th European Photovoltaic Solar Energy Conference 2014, 1132–1137). From the base area distribution, the pyramid height distribution was calculated using the known angle between opposite side walls of the pyramids, which is 70.5°.

SEM Measurements: A Schottky emission SEM model Auriga 60 (Zeiss) device was used to capture cross-sectional and top-view electron microscopy images. An angle of 45° was set to take top-view measurements. The acceleration voltage was set to 5 kV.

Spectrally Resolved PL Measurements: A LuQY Pro instrument (Quantum Yield Berlin) was used to conduct steady-state photoluminescence measurements. A 532 nm laser with an equivalent laser intensity set to approximately 1 sun (automatically calculated for the selected spot size as well as j_{SC} and EQE at 532 nm) was used to excite the perovskite absorber (resolution time to 3 s, spot size 0.1 cm^2).

PL-Based iV_{OC} Imaging: A measurement system developed at Fraunhofer ISE and built by Intego GmbH was used for the acquisition of PL images. The system was calibrated to allow absolute PL measurements that can be converted to iV_{OC} images. The perovskite silicon tandem solar cell can be excited subcell-selectively using a 450 nm laser and an 808 nm laser. The PL images were acquired using a silicon charge-coupled device camera and appropriate optical filters. The samples were illuminated before the image acquisition to reach stabilized conditions for measurements on perovskite sub-cells.

Suns-V_{OC} Measurements: The measurements were acquired at the same setup as the PL-based iV_{OC} imaging measurements were acquired at. The 450 and 808 nm lasers allow a subcell-selective excitation. A source meter connected to the cell measures the V_{OC} at various illumination intensities to acquire the pseudo-jV curves.

UV–vis Measurements: A lambda 950 spectrometer (PerkinElmer) tool was used to perform reflectance (R) and transmittance (T) measurements. Absorptance (A) was calculated by the formula $A = 1 - R - T$. Measurements were carried out in the wavelength range of 250–1200 nm with a 2 nm step size.

XRD: X-ray diffraction measurements were performed using a Bruker D8 Advance diffractometer. The tool was equipped with a Cu anode tube at 40 mA/40 kV. Measurements were carried out between $2\theta = 5°$ and $2\theta = 45°$. The step size was set at 0.03° and the time per step 0.1 s. Data analysis was done using the DIFRAC.EVA software.

TrPL: To record transient photoluminescence signals, the sample is excited with a 515 nm diode laser. The excitation spot size diameter is 7.5 mm. The pulse width is set to 240 µs ensuring steady state conditions of the charge carriers. The on/off ratio of the laser is 10^6 within 1 ns. The transient is recorded during the off time. The laser power during on-time was adjusted to match the j_{SC} of a perovskite solar cell under 1-sun illumination (AM 1.5G). The PL is registered with a VIS hybrid photodetector which is read out using single-photon counting device The integration time was set to 300 s.

jV Measurements: Current density–voltage measurements were carried out using a Wacom solar simulator equipped with two filtered light

© 2023 The Authors. Solar RRL published by Wiley-VCH GmbH

2367198x, 0, Downloaded from https://onlinelibrary.wiley.com/doi/10.1002/solr.202300659 by Fraunhofer Ise Inst. Solar Energy Systems, Wiley Online Library on [16/11/2023]. See the Terms and Conditions (https://onlinelibrary.wiley.com/terms-and-conditions) on Wiley Online Library for rules of use; OA articles are governed by the applicable Creative Commons License

sources, a halogen lamp, and a xenon lamp. Prior to the measurement, the spectral response was measured for the cell. Lamp intensities were then calculated following the procedure described by Meusel et al.[43] and adjusted with the help of two filtered WPVS reference solar cells. After calibration, the device was kept in OC conditions under illumination for 3 h at ambient conditions. Subsequently, *jV* curves were recorded using a Keithley 2400 source meter in forward and then reverse direction (range from –0.1 to 1.85 V, scan speed 34 mV s^{-1}, step width 20 mV). Between the single measurement points of the *jV* curve, the solar cell is under open-circuit condition. A shadow mask was used to limit light exposure area to the 1 cm^2 cell active area.

Spectrometric Characterization: Spectrometric characterization was performed on a light-emitting diode-based solar simulator (Wavelabs Sinus 220). The different spectra were calculated according to the procedure described by Chojniak et al.[64] For the spectrometric characterization, this procedure was adapted based on the definition of the parameter *z* according to ref. [43]. Before starting the measurement, the solar cell was kept under light for 3 h at ambient conditions. Then, *jV* curves were measured in reverse and forward scan (voltage range −0.2–1.9 V, 500 measurement points, sweep time 40 s per scan) for each spectrum alternating between redshifted and blueshifted spectral conditions starting from the AM1.5G condition outward. Before starting the *jV* scan, the cell was kept at V_{OC} during 250 s for each spectral condition.

EQE: The EQE was measured as described in our previous publication.[45]

Supporting Information

Supporting Information is available from the Wiley Online Library or from the author.

Acknowledgements

This work was funded by the Fraunhofer LIGHTHOUSE PROJECT MaNiTU as well as the German Federal Ministry for Economic Affairs and Climate Action under Contract No. 03EE1086A (PrEsto) as well as 03EE1087A and 03EE1087B (KATANA). The authors thank J. Zielonka for her support with SEM measurements, F. Martin for the support with *jV* measurements, K. Aborov and A. Gonzalez Abad for the support with EQE measurements, K. Zimmermann and H. Nagel for silicon bottom solar cell processing, and K. Fischer and J. Myers for technical support.

Open Access funding enabled and organized by Projekt DEAL.

Conflict of Interest

The authors declare no conflict of interest.

Data Availability Statement

The data that support the findings of this study are available from the corresponding author upon reasonable request.

Keywords

fully textured perovskite silicon tandem solar cells, loss analysis, optoelectronic simulation, photovoltaics, sentaurus technology computer-aided design

Received: August 18, 2023
Revised: October 16, 2023
Published online:

[1] M. H. Futscher, B. Ehrler, *ACS Energy Lett.* **2016**, *1*, 863.
[2] M. H. Futscher, B. Ehrler, *ACS Energy Lett.* **2017**, *2*, 2089.
[3] Z. Li, Y. Zhao, X. Wang, Y. Sun, Z. Zhao, Y. Li, H. Zhou, Q. Chen, *Joule* **2018**, *2*, 1559.
[4] N. L. Chang, J. Zheng, Y. Wu, H. Shen, F. Qi, K. Catchpole, A. Ho-Baillie, R. J. Egan, *Prog. Photovoltaics Res. Appl.* **2021**, *29*, 401.
[5] S. E. Sofia, H. Wang, A. Bruno, J. L. Cruz-Campa, T. Buonassisi, I. M. Peters, *Sustainable Energy Fuels* **2020**, *3*, 662.
[6] A. Al-Ashouri, E. Köhnen, B. Li, A. Magomedov, H. Hempel, P. Caprioglio, J. A. Márquez, A. B. Morales Vilches, E. Kasparavicius, J. A. Smith, N. Phung, D. Menzel, M. Grischek, L. Kegelmann, D. Skroblin, C. Gollwitzer, T. Malinauskas, M. Jošt, G. Matič, B. Rech, R. Schlatmann, M. Topič, L. Korte, A. Abate, B. Stannowski, D. Neher, M. Stolterfoht, T. Unold, V. Getautis, S. Albrecht, *Science* **2020**, *370*, 1300.
[7] J. Xu, C. C. Boyd, Z. J. Yu, A. F. Palmstrom, D. J. Witter, B. W. Larson, R. M. France, J. Werner, S. P. Harvey, E. J. Wolf, W. Weigand, S. Manzoor, M. F. A. M. van Hest, J. J. Berry, J. M. Luther, Z. C. Holman, M. D. McGehee, *Science* **2020**, *367*, 1097.
[8] F. Hou, Y. Li, L. Yan, B. Shi, N. Ren, P. Wang, D. Zhang, H. Ren, Y. Ding, Q. Huang, T. Li, Y. Li, Y. Zhao, X. Zhang, *Sol. RRL* **2021**, *5*, 2100357.
[9] A. Al-Ashouri, A. Magomedov, M. Roß, M. Jošt, M. Talaikis, G. Chistiakova, T. Bertram, J. A. Márquez, E. Köhnen, E. Kasparavičius, S. Levcenco, L. Gil-Escrig, C. J. Hages, R. Schlatmann, B. Rech, T. Malinauskas, T. Unold, C. A. Kaufmann, L. Korte, G. Niaura, V. Getautis, S. Albrecht, *Energy Environ. Sci.* **2019**, *12*, 3356.
[10] M. A. Mahmud, J. Zheng, S. Tang, G. Wang, J. Bing, A. D. Bui, J. Qu, L. Yang, C. Liao, H. Chen, S. P. Bremner, H. T. Nguyen, J. Cairney, A. W. Y. Ho-Baillie, *Adv. Energy Mater.* **2022**, *12*, 2201672.
[11] F. Sahli, J. Werner, B. A. Kamino, M. Bräuninger, R. Monnard, B. Paviet-Salomon, L. Barraud, L. Ding, J. J. Diaz Leon, D. Sacchetto, G. Cattaneo, M. Despeisse, M. Boccard, S. Nicolay, Q. Jeangros, B. Niesen, C. Ballif, *Nat. Mater.* **2018**, *17*, 820.
[12] G. Nogay, F. Sahli, J. Werner, R. Monnard, M. Boccard, M. Despeisse, F.-J. Haug, Q. Jeangros, A. Ingenito, C. Ballif, *ACS Energy Lett.* **2019**, *4*, 844.
[13] X. Luo, H. Luo, H. Li, R. Xia, X. Zheng, Z. Huang, Z. Liu, H. Gao, X. Zhang, S. Li, Z. Feng, Y. Chen, H. Tan, *Adv. Mater.* **2023**, *35*, 2207883.
[14] Q. Xu, B. Shi, Y. Li, L. Yan, W. Duan, Y. Li, R. Li, N. Ren, W. Han, J. Liu, Q. Huang, D. Zhang, H. Ren, S. Xu, C. Zhang, H. Zhuang, A. Lambertz, K. Ding, Y. Zhao, X. Zhang, *Adv. Energy Mater.* **2022**, *12*, 2202404.
[15] Y. Li, B. Shi, Q. Xu, L. Yan, N. Ren, Y. Chen, W. Han, Q. Huang, Y. Zhao, X. Zhang, *Adv. Energy Mater.* **2021**, *11*, 2102046.
[16] L. Mao, T. Yang, H. Zhang, J. Shi, Y. Hu, P. Zeng, F. Li, J. Gong, X. Fang, Y. Sun, X. Liu, J. Du, A. Han, L. Zhang, W. Liu, F. Meng, X. Cui, Z. Liu, M. Liu, *Adv. Mater.* **2022**, *34*, 2206193.
[17] Y. Hou, E. Aydin, M. de Bastiani, C. Xiao, F. H. Isikgor, D.-J. Xue, B. Chen, H. Chen, B. Bahrami, A. H. Chowdhury, A. Johnston, S.-W. Baek, Z. Huang, M. Wei, Y. Dong, J. Troughton, R. Jalmood, A. J. Mirabelli, T. G. Allen, E. van Kerschaver, M. I. Saidaminov, D. Baran, Q. Qiao, K. Zhu, S. de Wolf, E. H. Sargent, *Science* **2020**, *367*, 1135.
[18] F. H. Isikgor, F. Furlan, J. Liu, E. Ugur, M. K. Eswaran, A. S. Subbiah, E. Yengel, M. de Bastiani, G. T. Harrison, S. Zhumagali, C. T. Howells, E. Aydin, M. Wang, N. Gasparini, T. G. Allen, A. U. Rehman, E. van Kerschaver, D. Baran, I. McCulloch, T. D. Anthopoulos, U. Schwingenschlögl, F. Laquai, S. de Wolf, *Joule* **2021**, *5*, 1566.

© 2023 The Authors. Solar RRL published by Wiley-VCH GmbH

2367198x, 0, Downloaded from https://onlinelibrary.wiley.com/doi/10.1002/solr.202300659 by Fraunhofer Ise Inst. Solar Energy Systems, Wiley Online Library on [16/11/2023]. See the Terms and Conditions (https://onlinelibrary.wiley.com/terms-and-conditions) on Wiley Online Library for rules of use; OA articles are governed by the applicable Creative Commons License

[19] P. Tockhorn, J. Sutter, A. Cruz, P. Wagner, K. Jäger, D. Yoo, F. Lang, M. Grischek, B. Li, J. Li, O. Shargaieva, E. Unger, A. Al-Ashouri, E. Köhnen, M. Stolterfoht, D. Neher, R. Schlatmann, B. Rech, B. Stannowski, S. Albrecht, C. Becker, *Nat. Nanotechnol.* **2022**, *17*, 1214.
[20] A. Harter, S. Mariotti, L. Korte, R. Schlatmann, S. Albrecht, B. Stannowski, *Prog. Photovoltaics* **2023**, *31*, 813.
[21] J. Zheng, H. Wei, Z. Ying, X. Yang, J. Sheng, Z. Yang, Y. Zeng, J. Ye, *Adv. Energy Mater.* **2023**, *13*, 2203006.
[22] NREL, *Best Research-Cell Efficiency Chart*, https://www.nrel.gov/pv/interactive-cell-efficiency.html.
[23] A. Farag, P. Fassl, H. Hu, T. Feeney, A. Quintilla, M. A. Ruiz-Preciado, W. Hempel, D. Bagrowski, P. Noack, B. Wattenberg, T. Dippell, U. W. Paetzold, *Adv. Funct. Mater.* **2023**, *33*, 2210758.
[24] A. J. Bett, D. Chojniak, M. Schachtner, S. K. Reichmuth, Ö. Ş. Kabaklı, P. S. C. Schulze, O. Fischer, F. Schindler, J. Hohl-Ebinger, G. Siefer, M. C. Schubert, *Sol. RRL* **2023**, *7*, 2200948.
[25] F. Lang, E. Köhnen, J. Warby, K. Xu, M. Grischek, P. Wagner, D. Neher, L. Korte, S. Albrecht, M. Stolterfoht, *ACS Energy Lett.* **2021**, *6*, 3982.
[26] M. Boccard, C. Ballif, *ACS Energy Lett.* **2020**, *5*, 1077.
[27] Y. H. Zeng, Z. T. Ding, Z. K. Liu, W. Liu, M. D. Liao, X. Yang, Z. Q. Ying, J. S. Sun, J. Sheng, B. J. Yan, H. Y. He, C. H. Shou, Z. H. Yang, J. C. Ye, *J. Semicond.* **2023**, *44(8)*, 082702, https://doi.org//10.1088/1674-4926/44/8/082702.
[28] K. Jäger, J. Sutter, M. Hammerschmidt, P.-I. Schneider, C. Becker, *Nanophotonics* **2021**, *10*, 1991, https://doi.org/10.1515/nanoph-2020-0674.
[29] O. Er-raji, L. Rustam, B. P. Kore, S. W. Glunz, P. S. C. Schulze, *ACS Appl. Energy Mater.* **2023**, *6*, 6183.
[30] X. Y. Chin, D. Turkay, J. A. Steele, S. Tabean, S. Eswara, M. Mensi, P. Fiala, C. M. Wolff, A. Paracchino, K. Artuk, D. Jacobs, Q. Guesnay, F. Sahli, G. Andreatta, M. Boccard, Q. Jeangros, C. Ballif, *Science* **2023**, *381*, 59.
[31] F. Zhang, B. Tu, S. Yang, K. Fan, Z. Liu, Z. Xiong, J. Zhang, W. Li, H. Huang, C. Yu, K. Yao, A. K.-Y. Jen, *Adv. Mater.* **2023**, *35*, 2303139.
[32] A. Onno, C. Reich, S. Li, A. Danielson, W. Weigand, A. Bothwell, S. Grover, J. Bailey, G. Xiong, D. Kuciauskas, W. Sampath, Z. C. Holman, *Nat. Energy* **2022**, *7*, 400.
[33] O. Fischer, A. D. Bui, F. Schindler, D. Macdonald, S. W. Glunz, H. T. Nguyen, M. C. Schubert, *Prog. Photovoltaics* **2023**, https://doi.org//10.1002/PIP.3754.
[34] S. Rühle, *Sol. Energy* **2016**, *130*, 139.
[35] S. Gharibzadeh, P. Fassl, I. M. Hossain, P. Rohrbeck, M. Frericks, M. Schmidt, T. Duong, M. R. Khan, T. Abzieher, B. A. Nejand, F. Schackmar, O. Almora, T. Feeney, R. Singh, D. Fuchs, U. Lemmer, J. P. Hofmann, S. A. L. Weber, U. W. Paetzold, *Energy Environ. Sci.* **2021**, *14*, 5875.
[36] J. Liu, M. de Bastiani, E. Aydin, G. T. Harrison, Y. Gao, R. R. Pradhan, M. K. Eswaran, M. Mandal, W. Yan, A. Seitkhan, M. Babics, A. S. Subbiah, E. Ugur, F. Xu, L. Xu, M. Wang, A. U. Rehman, A. Razzaq, J. Kang, R. Azmi, A. A. Said, F. H. Isikgor, T. G. Allen, D. Andrienko, U. Schwingenschlögl, F. Laquai, S. de Wolf, *Science* **2022**, *377*, 302.
[37] P. Caprioglio, F. Zu, C. M. Wolff, J. A. Márquez Prieto, M. Stolterfoht, P. Becker, N. Koch, T. Unold, B. Rech, S. Albrecht, D. Neher, *Sustainable Energy Fuels* **2019**, *3*, 550.
[38] M. Stolterfoht, P. Caprioglio, C. M. Wolff, J. A. Márquez, J. Nordmann, S. Zhang, D. Rothhardt, U. Hörmann, Y. Amir, A. Redinger, L. Kegelmann, F. Zu, S. Albrecht, N. Koch, T. Kirchartz, M. Saliba, T. Unold, D. Neher, *Energy Environ Sci.* **2019**, *12*, 2778.
[39] J. Warby, F. Zu, S. Zeiske, E. Gutierrez-Partida, L. Frohloff, S. Kahmann, K. Frohna, E. Mosconi, E. Radicchi, F. Lang, S. Shah, F. Peña-Camargo, H. Hempel, T. Unold, N. Koch, A. Armin, F. de Angelis, S. D. Stranks, D. Neher, M. Stolterfoht, *Adv. Energy Mater.* **2022**, *12*, 2103567.
[40] U. Wurfel, A. Cuevas, P. Wurfel, *IEEE J. Photovoltaics* **2015**, *5*, 461.
[41] D. Pysch, C. Meinhard, N.-P. Harder, M. Hermle, S. W. Glunz, *J. Appl. Phys.* **2011**, *110*, 94516.
[42] O. Er-raji, A. Bett, S. Lange, H. Nagel, M. Bivour, O. Schultz-Wittmann, C. Hagendorf, M. Hermle, J. Borchert, S. Glunz, P. Schulze, *Prog. Photovoltaics* **2023**, submitted to.
[43] M. Meusel, R. Adelhelm, F. Dimroth, A. W. Bett, W. Warta, *Prog. Photovoltaics Res. Appl.* **2002**, *10*, 243.
[44] Ö. Ş. Kabaklı, J. Kox, L. Tutsch, M. Heydarian, A. J. Bett, S. Lange, O. Fischer, C. Hagendorf, M. Bivour, M. Hermle, P. S. Schulze, J. C. Goldschmidt, *EuroSun2004* **2023**, *254*, 112246.
[45] M. Heydarian, C. Messmer, A. J. Bett, M. Heydarian, D. Chojniak, Ö. Ş. Kabaklı, L. Tutsch, M. Bivour, G. Siefer, M. C. Schubert, J. C. Goldschmidt, M. Hermle, S. W. Glunz, P. S. C. Schulze, *Sol. RRL* **2023**, *7*, 2200930.
[46] C. Messmer, D. Chojniak, A. Bett, K. Reichmuth, J. Hohl-Ebinger, M. Bivour, M. Hermle, J. Schön, M. Schubert, S. W. Glunz, *Prog. Photovoltaics*, submitted to.
[47] A. Callies, M. Hanser, J. C. Goldschmidt, B. Bläsi, O. Höhn, *Opt. Express* **2023**, *31*, 19428.
[48] Sentaurus TCAD, *Technology Computer Aided Design (TCAD)*, Synopsys, Zürich, Switzerland, release U-2022.12-SP1.
[49] C. Messmer, B. S. Goraya, S. Nold, P. S. Schulze, V. Sittinger, J. Schön, J. C. Goldschmidt, M. Bivour, S. W. Glunz, M. Hermle, *Prog. Photovoltaics* **2020**, *29*, 744.
[50] C. Messmer, J. Schn, U. Wrfel, P. S. C. Schulze, M. C. Schubert, M. Bivour, S. W. Glunz, M. Hermle, *Efficient Charge Carrier Extraction in Perovskite-Silicon Tandem Solar Cells Investigated by Numerical Simulation*, presented at the 8th World Conference on Photovoltaic Energy Conversion, 26–30 September 2022, Milan, Italy, https://doi.org//10.4229/WCPEC-82022-2BV.2.40.
[51] C. Messmer, J. Schön, S. Lohmüller, J. Greulich, C. Luderer, J. C. Goldschmidt, M. Bivour, S. W. Glunz, M. Hermle, *Prog. Photovoltaics Res. Appl.* **2022**, *30*, 1023.
[52] M. Meusel, C. Baur, G. Létay, A. W. Bett, W. Warta, E. Fernandez, *Prog. Photovoltaics Res. Appl.* **2003**, *11*, 499.
[53] V. Sittinger, P. S. C. Schulze, C. Messmer, A. Pflug, J. C. Goldschmidt, *Opt. Express* **2022**, *30*, 37957.
[54] D. Menzel, A. Al-Ashouri, A. Tejada, I. Levine, J. A. Guerra, B. Rech, S. Albrecht, L. Korte, *Adv. Energy Mater.* **2022**, *12*, 2201109.
[55] C. Messmer, L. Tutsch, S. Pingel, D. Erath, J. Schön, A. Fell, J. C. Goldschmidt, B. S. Goraya, F. Clement, A. Lorenz, S. Nold, M. Bivour, S. W. Glunz, M. Hermle, *Prog. Photovoltaics* **2022**, *30*, 374.
[56] W. Shockley, H. J. Queisser, *J. Appl. Phys.* **1961**, *32*, 510.
[57] I. Almansouri, A. Ho-Baillie, M. A. Green, *Jpn. J. Appl. Phys.* **2015**, *54*, 8.
[58] T. Niewelt, B. Steinhauser, A. Richter, B. Veith-Wolf, A. Fell, B. Hammann, N. E. Grant, L. Black, J. Tan, A. Youssef, J. D. Murphy, J. Schmidt, M. C. Schubert, S. W. Glunz, *EuroSun2004* **2022**, *235*, 111467.
[59] Q. Jiang, J. Tong, Y. Xian, R. A. Kerner, S. P. Dunfield, C. Xiao, R. A. Scheidt, D. Kuciauskas, X. Wang, M. P. Hautzinger, R. Tirawat, M. C. Beard, D. P. Fenning, J. J. Berry, B. W. Larson, Y. Yan, K. Zhu, *Nature* **2022**, *611*, 278.

© 2023 The Authors. Solar RRL published by Wiley-VCH GmbH

2367198x, 0, Downloaded from https://onlinelibrary.wiley.com/doi/10.1002/solr.202300659 by Fraunhofer Ise Inst. Solar Energy Systems, Wiley Online Library on [16/11/2023]. See the Terms and Conditions (https://onlinelibrary.wiley.com/terms-and-conditions) on Wiley Online Library for rules of use; OA articles are governed by the applicable Creative Commons License

[60] C. Xu, Z. Zhang, S. Zhang, H. Si, S. Ma, W. Fan, Z. Xiong, Q. Liao, A. Sattar, Z. Kang, Y. Zhang, *Adv. Funct. Mater.* **2021**, *31*, 2009425.
[61] I. Levine, A. Al-Ashouri, A. Musiienko, H. Hempel, A. Magomedov, A. Drevilkauskaite, V. Getautis, D. Menzel, K. Hinrichs, T. Unold, S. Albrecht, T. Dittrich, *Joule* **2021**, *5*, 2915.
[62] Z. Liu, J. Siekmann, B. Klingebiel, U. Rau, T. Kirchartz, *Adv. Energy Mater.* **2021**, *11*, 2003386.
[63] L. Xu, J. Liu, K. McIntosh, M. Abbott, E. Aydin, T. Allen, M. de Bastiani, M. Babics, J. Kang, M. Alamer, W. Yan, W. Liu, F. Xu, A. U. Rehman, S. de Wolf, *PRX Energy 1* **2022**, *1*, 023005, https://doi.org/10.1103/PRXEnergy.1.023005.
[64] *AIP Conf. Proc.* (Eds: D Chojniak, A. J. Bett, J. Hohl-Ebinger, S. K. Reichmuth, M. Schachtner, G. Siefer), *AIP Conf. Proc.*, vol. *2826*, 030003 **2023**, https://doi.org/10.1063/5.0140990.

© 2023 The Authors. Solar RRL published by Wiley-VCH GmbH

2367198x, 0, Downloaded from https://onlinelibrary.wiley.com/doi/10.1002/solr.202300659 by Fraunhofer Ise Inst. Solar Energy Systems, Wiley Online Library on [16/11/2023]. See the Terms and Conditions (https://onlinelibrary.wiley.com/terms-and-conditions) on Wiley Online Library for rules of use; OA articles are governed by the applicable Creative Commons License

View publication stats